

Imaging Local Electric Field Distribution by Plasmonic Impedance Microscopy

Yixian Wang, Xiaonan Shan, Shaopeng Wang, and Nongjian Tao*

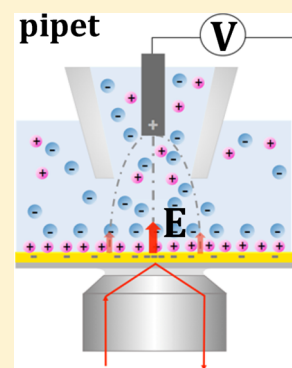
Center for Bioelectronics and Biosensors, Biodesign Institute, Arizona State University, Tempe, Arizona 85287, United States

Pierre-Yves Blanchard, Keke Hu, and Michael V. Mirkin*

Department of Chemistry and Biochemistry, Queens College—CUNY, Flushing, New York 11367, United States,

S Supporting Information

ABSTRACT: We report on imaging of local electric field on an electrode surface with plasmonic electrochemical impedance microscopy (P-EIM). The local electric field is created by putting an electrode inside a micropipet positioned over the electrode and applying a voltage between the two electrodes. We show that the distribution of the surface charge as well as the local electric field at the electrode surface can be imaged with P-EIM. The spatial distribution and the dependence of the local charge density and electric field on the distance between the micropipet and the surface are measured, and the results are compared with the finite element calculations. The work also demonstrates the possibility of integrating plasmonic imaging with scanning ion conductance microscopy (SICM) and other scanning probe microscopies.



Measuring local surface charge and related local electric field on or near an electrode surface is important for studying basic surface electrochemical phenomena and characterizing electrode materials relevant to nanoscience, energy research, and bioelectrochemistry applications.^{1–8} The Bard group demonstrated a scanning electrochemical microscopy (SECM) capability for measuring local surface charge changes induced by oxidation/reduction of adsorbed species on the portion of the substrate facing the tip.^{9,10} Unwin et al. recently reported imaging of surface charge based on the interaction between the double layer of a nanopipet and the surface charge.^{11,12} Both approaches used scanning probe microscopy (SECM or scanning ion conductance microscopy (SICM)), involving detection of current and conversion of the current to charge.

Here we present imaging of surface charge (electric field) at the surface of a substrate electrode with a plasmonics-based electrochemical impedance imaging (P-EIM) technique. The local electric field is generated with an electrode in a micropipet posited near the electrode, analogous to SICM.^{11–19} Unlike a typical SICM, where a voltage is applied between the micropipet electrode and another electrode in electrolyte, we apply a voltage between the micropipet electrode and the substrate electrode, which induces local surface charge (electric field) at the substrate surface. Another difference between the SICM (or SECM) and P-EIM is that P-EIM images the local electric field (or charge) distribution optically based on the sensitive dependence of surface plasmon resonance on surface charge density. Previously, we imaged local electrochemical

reactions and interfacial impedance with P-EIM.^{20–30} In the present work, we extend these efforts by integrating the plasmonic imaging approach and the scanning probe microscopy configuration into a single setup.

Figure 1A is a schematic illustration of the experimental setup, where a micropipet (with a Ag/AgCl electrode inside) is placed above a substrate electrode made of a glass slide coated with 47 nm thick gold film. The distance between the micropipet tip and the substrate electrode is controlled with a piezo-electric transducer. The substrate electrode is placed on a high numerical aperture oil emersion objective with refractive index matching oil. Light from a superluminescence diode (SLD) is directed on the gold surface via the objective with a proper incident angle to excite surface plasmons, and the reflected light is collected by the same objective and directed to a CCD camera to record plasmonic images. A voltage is applied between the micropipet and substrate electrodes to induce charge (electric field) on the substrate electrode, and the charge (electric field) distribution is mapped with the plasmonic imaging setup. In order to accurately map the charge and surface electric field distributions, the voltage is modulated periodically, and the plasmonic image intensity at each pixel is analyzed with fast Fourier transform (FFT) in time domain to extract a dc (zero frequency) and ac (periodic modulation at the frequency of applied voltage) signals. The dc signal is the

Received: November 18, 2015

Accepted: December 28, 2015

Published: December 28, 2015

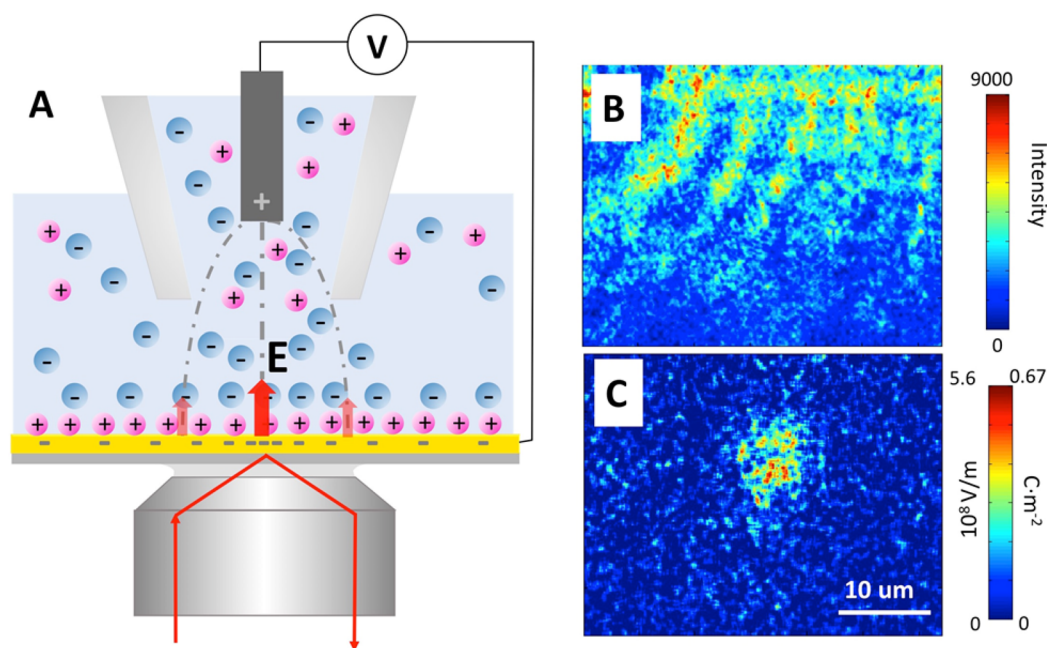


Figure 1. (A) Schematic of the setup, where dashed lines represent the electric field distribution, and the red arrows indicate the local electric field on the substrate surface (within the double layer) measured by P-EIM. (B) dc and (C) ac amplitude images of a 6.3 μm -diameter pipet induced surface charge distribution on Au electrode.

conventional surface plasmon resonance image, and the ac signal has two components, amplitude and phase, providing local electric field and charge distribution images.

Using this setup, we imaged the local charge and electric field distributions at the gold electrode induced by micropipets with different orifice diameters, studied the dependence of the distributions on the distance between the micropipet tip and gold electrode, and compared the results with theoretical simulations.

EXPERIMENTAL SECTION

Chemicals. Phosphate buffered saline (Corning cellgro, 154 mM NaCl, 5.6 mM Na_2HPO_4 , and 1.1 mM KH_2PO_4) was used either as received or diluted with deionized water (Milli-Q, Millipore Corp.) by six times before usage.

Fabrication of Micropipets. Micropipets were fabricated by pulling borosilicate capillaries (o.d./i.d. ratio of 1.5/0.86; Sutter Instrument Co., Novato, CA) with a heating pipet puller (P-97, Sutter Instrument Co.).

Instrumentation. The imaging setup was built on an inverted microscope (Olympus IX-81) equipped with a high numerical aperture oil-emersion objective. P-polarized light from a 670 nm SLD (SLD-260-MP, Superlum) was used as light source, and a CCD camera (Pike F-032, Allied Vision) was used for imaging. The gold substrate electrodes were prepared by coating 47 nm gold onto glass coverslips using method described elsewhere.²² The potentials of the micropipet and gold electrodes were controlled with a potentiostat (Autolab) or bipotentiostat (ARFDES, Pine), and a function generator (33521A, Agilent) was used to apply potential modulation with frequency of 5 and 20 Hz and amplitude varying from 100 to 400 mV. The local surface charge and electric field images were obtained with imaging processing algorithms implemented with Matlab (R2013b, MathWorks).

Positioning of the Micropipet. The x , y , and z positions of the micropipet were coarsely controlled with a three-axis

manual translation stage (PT3, Thorlab) under the guidance of transmitted image using the same objective and camera as those for P-EIM but with a LED (MS05L3, Thorlab) mounted on top of the inverted microscope as a light source. The z position, or the distance between the micropipet and the substrate electrode, was finely controlled with a piezoelectric transducer (NFLSDP20S, Thorlab; 30 μm travel range with 1 nm increment) controlled by a T-cube Piezo Controller (TPZ001, Thorlab) in a closed loop feedback configuration. A T-cube strain gauge reader was used to read the distance, where zero distance was determined when the micropipet began to “touch” the substrate surface as observed by a sudden increase in the contrast of the plasmonic image.

Data Extraction and Processing. The raw P-EIM images were batch-converted to 16-bit tiff format files using a Matlab program. The first image was subtracted from all the subsequent frames and then smoothed over 5×5 pixels. The ac amplitude images were obtained by performing FFT to every pixel in time domain.

COMSOL Simulations. Numerical simulations were carried out by coupling the Electrostatics and Transport of Diluted Species modules in COMSOL 4.4. A simulation report, including equations and boundary conditions, is provided in the [Supporting Information](#).

RESULTS AND DISCUSSION

Electric Field Mapping. Plasmonic imaging of local electric field distribution is based on that the surface plasmon resonance condition, such as resonant angle, is sensitive to the surface charge. We have shown previously that the surface charge density change ($\Delta\sigma$) is directly proportional to the resonant angle shift ($\Delta\theta_R$) given by^{27,28}

$$\Delta\sigma = \alpha \Delta\theta_R \quad (1)$$

where $\alpha \approx 28 \text{ C m}^{-2} \text{ deg}^{-1}$ is a constant that can be calibrated experimentally or estimated theoretically based on the dielectric

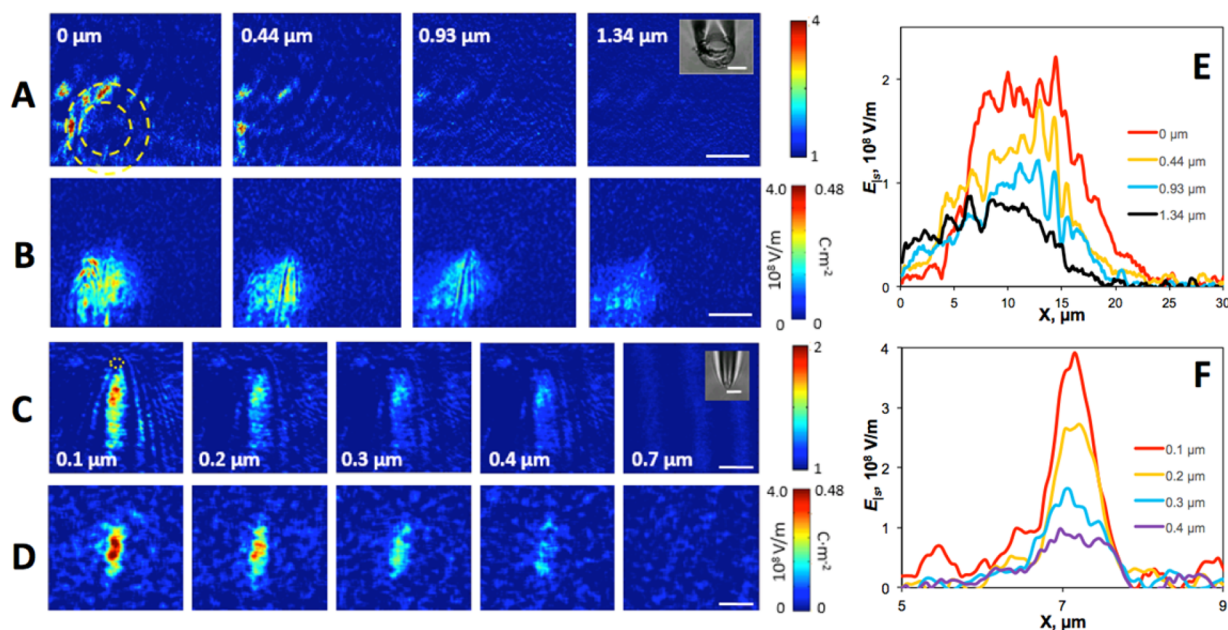


Figure 2. dc (A, C) and ac (B, D) images for a 11 μm - (A, B) and a 0.67 μm -diameter (C, D) micropipets at different separation distances. Insets are the bright field optical images of the micropipets. The scale bars are 10 μm for parts A and B and 2 μm for parts C and D, respectively. The amplitudes in dc images are normalized by the image recorded when the micropipet is far away from the substrate surface such that the micropipet does not contribute to the plasmonic image contrast. The yellow dashed circles in parts A and C represent the location of the micropipet tips. The potential modulation amplitude and frequency are 0.3 V and 5 Hz, respectively, for parts A and B and 0.4 V and 20 Hz for parts C and D. The electrolyte is 6 \times diluted PBS for parts A and B and original PBS for parts C and D. Line profiles of electric field distribution in lateral direction of the 11 μm -diameter micropipet (E) and the 0.67 μm -diameter micropipet (F) at different distances.

property of the metal film (gold). The detailed derivation of the equation can be found in ref 28. $\Delta\theta_R$ is determined from the plasmonic image intensity. According to Gauss's Law, the electric field on the substrate surface (E_s) is normal to the electrode surface and related to the electrode surface charge density according to

$$E_s = \frac{\sigma}{\epsilon\epsilon_0} \quad (2)$$

where ϵ and ϵ_0 are the dielectric constant of the medium and vacuum permittivity, respectively. From the surface charge density measured from the plasmonic image, eq 2 allows us to determine the electric field distribution on the gold surface.

Note that E_s in eq 2 is the electric field on the surface, which is determined solely by the substrate surface charge density. The electric field in the electrolyte (dashed lines in Figure 1) is determined not only by the surface charge density but also by the ionic distribution in the electrolyte, which is not measured by P-EIM but can be simulated by solving Poisson–Boltzmann equation or more sophisticated model with proper boundary conditions (see COMSOL simulations below).

Using the setup sketched in Figure 1A, we obtained both the dc and ac components of the plasmonic image of a 6.3 μm diameter micropipet brought within $\sim 1 \mu\text{m}$ from the substrate electrode. The dc plasmonic image (Figure 1B) shows little contrast, which can be explained by the following considerations. The dc plasmonic image contrast of an object arises from the scattering of the plasmonic wave by the object within the evanescent optical field associated with the wave. The evanescent field decays exponentially from the electrode surface with a decay constant of $\sim 100 \text{ nm}$,³¹ which becomes negligibly small at $\sim 1 \mu\text{m}$ from the substrate electrode, where the micropipet tip is located. Consequently, the dc plasmonic

image contrast of the micropipet is weak and within the noise level. Moving the micropipet closer to the surface does lead to an increase in the contrast of the dc plasmonic image of the micropipet (we will return to this later). Unlike the dc image, the ac amplitude image (Figure 1C) shows a clear spot, which represents the local electric field distribution created by the micropipet on the substrate surface. This example shows that an object (micropipet) outside of the evanescent field can be imaged in the ac image as long as it can produce a detectable change in the surface charge or electric field on the substrate electrode (SPR chip).

We studied the dependence of the electric field distribution on the distance between the tip of a micropipet and the substrate electrode. Figure 2A shows dc plasmonic images of a micropipet (diameter of 11 μm) at various distances. When the micropipet is close to the substrate electrode surface, the dc plasmonic image shows several bright spots (dashed circles in Figure 2A) arising from the scattering of surface plasmonic waves by the rough surface of the micropipet tip. As the distance increases, the dc plasmonic image contrast decreases as we expect from the exponential decay of the evanescent field associated with the plasmonic wave. A similar decrease of the dc plasmonic image contrast was observed also for a 0.67 μm -diameter micropipet (Figure 2C). Unlike the 11- μm micropipet, the dc plasmonic image of the 0.67- μm micropipet shows a parabolic tail, which is a characteristic feature of plasmonic wave scattering by a small object (smaller than the wavelength of the plasmonic wave).³²

The corresponding surface electric field (and charge density) images of the 11- μm and 0.67- μm micropipets at various distances were obtained from the ac component of the plasmonic images. Both pipets generate local electric field on the planar electrode, and the bright area in the images

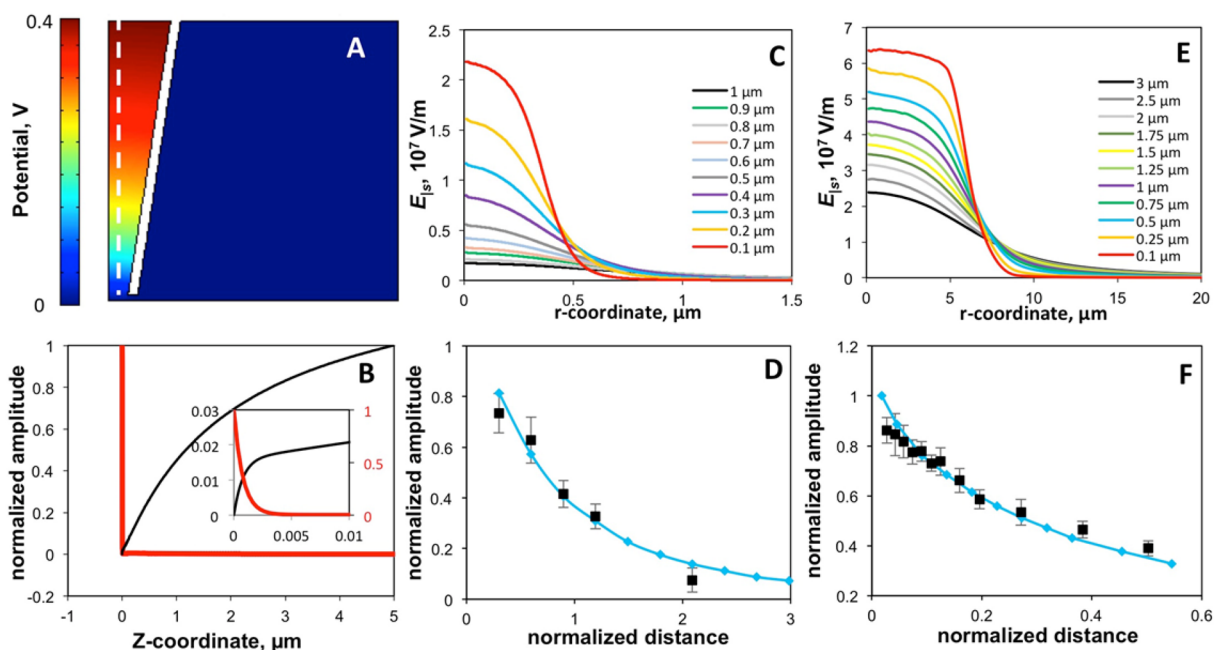


Figure 3. Numerical simulation of potential and electric field distributions vs micropipet–substrate distance and comparison with experimental data. (A) Simulated potential distribution inside and outside of a micropipet. (B) Simulated line profiles of potential (black) and electric field (red) distributions along the white dashed line in part A, where the inset shows the zoom-in of the profiles close to the substrate surface. (C) Simulated line profiles of electric field distribution along the radial direction at different distances. (D) Comparison between experimental (black squares with error bar) and simulated (blue diamonds with a blue line) averaged electric fields on the substrate electrode underneath the pipet orifice. The diameter of the micropipet orifice in parts A–D is $0.67\ \mu\text{m}$. (E) Simulated line profiles of electric field distribution along the radial direction at different distances for an $11\text{-}\mu\text{m}$ diameter micropipet. (F) Comparison between experimental (black squares with error bar) and simulated (blue diamonds with a blue line) averaged electric fields on the substrate electrode underneath the pipet orifice for an $11\text{-}\mu\text{m}$ diameter micropipet.

corresponds with the shape of the pipet orifice. The elongated shape from the smaller pipet is due to the propagation of surface plasmon wave,^{23,33} which is not obvious for a larger object. Both the electric field and dc plasmonic images show decrease in the image contrast with the distance, but the decrease of the electric field image contrast with the distance is slower than that of the dc plasmonic image. This difference in distance dependence is due to that the dependence in the imaging mechanisms between the dc and ac plasmonic images. The former arises from the scattering of the micropipet tip by the surface plasmonic wave, which is determined by the decay of the evanescent wave. In contrast the latter is due to the surface charge density on the substrate electrode created by the micropipet, which decreases with the distance due to electrostatics. From the ac images, we extracted the line profiles of the electric field distribution of these micropipets at different micropipet–electrode surface distances (Figure 2E,F), which provides a more quantitative view of the surface field (charge) distributions.

COMSOL Simulations. To further validate the experimental results, we carried out numerical simulations (see the Supporting Information for simulation details). To simulate the electric field distribution on the substrate electrode, we need to consider the field and ion distributions in the electrolyte, including the diffuse double layer and the geometry of the micropipet. For this purpose, we coupled the Nernst–Planck equations to the Poisson–Boltzmann equation. The Nernst–Planck equations were solved for the distributions of the ions using the Transport of Diluted Species physics module, and the Poisson’s equation was solved for the potential using the Electrostatics physics module.

When a constant voltage is applied between the micropipet and substrate electrodes, almost all the potential drops across the double layer region and there is no image contrast in the area underneath the pipet (Figure S4). When ac modulation is applied between the two electrodes, the system can be modeled as an electrolyte resistance and a double layer impedance in series. The ratio between the two determines the potential drop throughout the electrolyte. The electrolyte resistance mostly comes from the region within the micropipet, which depends on the conductivity of the electrolyte and the geometry of the micropipet including both the radius and angle.³⁴ Because of the computational limit in the simulation, we simulated a much smaller area than the actual substrate electrode area. To compensate this limitation, we increased the oscillation frequency such that the total impedance is the same as the actual surface impedance. This is possible because the impedance of the double layer is reversely proportional to the product of frequency and capacitance.

The potential and electric distributions inside and outside of a $0.67\ \mu\text{m}$ -micropipet simulated with the method described above are shown in Figure 3A,B. The simulation also provides the distance dependence of the local electric field on the substrate along the radial coordinate, which is an experimentally measurable parameter (Figure 3C,E). As mentioned previously, we increased the applied modulation frequency to compensate the smaller electrode area in the simulation. The frequencies were set to be 5×10^6 and 1.25×10^5 Hz, for the $0.67\text{-}\mu\text{m}$ and $11\text{-}\mu\text{m}$ micropipets, respectively. The simulated field distributions (Figure 3C,E) and experimental field distributions (Figure 2E,F) on the substrate surface are in good agreement although the field strengths in the simulations are smaller (~ 20 times smaller for the $0.67\text{-}\mu\text{m}$ micropipet and ~ 2 times smaller for

the 11- μm one). This discrepancy may be attributed to the high frequencies used in the simulation, which compensate the underestimated capacitance (surface area), but the ions may not fully follow the potential modulations at the high frequencies. To quantify the distance dependence of the local electric field, we determined the averaged electric field strengths underneath the micropipet orifice vs the distance obtained from the simulations and experiments, which are in excellent agreement (Figure 3D,F).

In the experiments discussed above, we applied a voltage between the micropipet and substrate electrodes, which is in contrast to a typical SICM experiment, where the potential of a micropipet electrode is controlled with respect to a separate reference electrode in the electrolyte. We also performed the measurement by controlling the micropipet potential with respect to a reference electrode with the substrate electrode potential left floating and observed qualitatively similar distribution and distance dependence of the electric field on the substrate surface (see the Supporting Information).

CONCLUSIONS

A micropipet in a scanning probe microscope (e.g., SICM) can be integrated into a plasmonic microscope. By applying an oscillating potential to the micropipet positioned near a substrate electrode, charge is induced on the electrode surface, which leads to a dc and ac plasmonic images. The dc image measures the scattering of the surface plasmonic waves by the micropipet, which provides the location and size information on the micropipet tip. In contrast, the ac plasmonic image maps the surface charge density distribution, from which the electric field on the substrate surface is obtained. The field and its distribution depend on the micropipet–substrate distance and the size of the orifice of the micropipet, and these dependences are in agreement with numerical simulations. Although the present experiments used relatively large (0.67 and 11 μm diameters) micropipet orifices, the experimental technique can be applied to nanosized pipet orifices. We anticipate that the integrated plasmonic and scanning probe microscope setup can combine the strengths of fast imaging of plasmonic technique with the local probe capability of SICM and SECM for studying various electrochemical processes on electrodes.

ASSOCIATED CONTENT

Supporting Information

The Supporting Information is available free of charge on the ACS Publications website at DOI: 10.1021/acs.analchem.5b04382.

Additional figures and COMSOL simulations (PDF)

AUTHOR INFORMATION

Corresponding Authors

*E-mail: njtao@asu.edu.

*E-mail: Michael.Mirkin@qc.cuny.edu.

Notes

The authors declare no competing financial interest.

ACKNOWLEDGMENTS

This work is support by AFOSR (Grant FA9550-14-1-0003) and NIH (Grant 5R01GM107165).

REFERENCES

(1) Heinz, W. F.; Hoh, J. H. *Biophys. J.* **1999**, *76*, 528–538.

(2) Butt, H.-J. *Biophys. J.* **1992**, *63*, 578–582.

(3) Morkved, T. L.; Lu, M.; Urbas, A. M.; Ehrlich, E. E.; Jaeger, H. M.; Mansky, P.; Russell, T. P. *Science* **1996**, *273*, 931–933.

(4) Lust, E.; Janes, A.; Sammelselg, V.; Miidla, P. *Electrochim. Acta* **2000**, *46*, 185–191.

(5) Gwo, S.; Yeh, C.-L.; Chen, P.-F.; Chou, Y.-C.; Chen, T. T.; Chao, T.-S.; Hu, S.-F.; Huang, T.-Y. *Appl. Phys. Lett.* **1999**, *74*, 1090–1092.

(6) Asamoah, O. K.; Wuskell, J. P.; Loew, L. M.; Bezanilla, F. *Neuron* **2003**, *37*, 85–97.

(7) Corovic, S.; Pavlin, M.a; Miklavcic, D. *Biomed. Eng. Online* **2007**, *6*, 37.

(8) Schkolnik, G.; Utesch, T.; Salewski, J.; Tenger, K.; Millo, D.; Kranich, A.; Zebger, I.; Schulz, C.; Zimanyi, L.; Rakhely, G.; Mroginiski, M. A.; Hildebrandt, P. *Chem. Commun.* **2012**, *48*, 70–72.

(9) Rodríguez-López, J.; Alpuche-Avilés, M. A.; Bard, A. J. *J. Am. Chem. Soc.* **2008**, *130*, 16985–16995.

(10) Wang, Q.; Rodríguez-López, J.; Bard, A. J. *J. Am. Chem. Soc.* **2009**, *131*, 17046–17047.

(11) McKelvey, K.; Kinnear, S. L.; Perry, D.; Momotenko, D.; Unwin, P. R. *J. Am. Chem. Soc.* **2014**, *136*, 13735–13744.

(12) Perry, D.; Al Botros, R.; Momotenko, D. S.; Kinnear, L.; Unwin, P. R. *ACS Nano* **2015**, *9*, 7266–7276.

(13) Chen, C.-C.; Zhou, Y.; Baker, L. A. *Annu. Rev. Anal. Chem.* **2012**, *5*, 207–228.

(14) Novak, P.; Li, C.; Shevchuk, A. I.; Stepanyan, R.; Caldwell, M.; Hughes, S.; Smart, T. G.; Gorelik, J.; Ostanin, V. P.; Lab, M. J.; Moss, G. W. J.; Frolenkov, G. I.; Klenerman, D.; Korchev, Y. E. *Nat. Methods* **2009**, *6*, 279–281.

(15) Chen, C.-C.; Derylo, M. A.; Baker, L. A. *Anal. Chem.* **2009**, *81*, 4742–4751.

(16) Korchev, Y. E.; Negulyaev, Y. A.; Edwards, C. R. W.; Vodyanoy, I.; Lab, M. J. *Nat. Cell Biol.* **2000**, *2*, 616–619.

(17) Takahashi, Y.; Shevchuk, A. I.; Novak, P.; Zhang, Y.; Ebejer, N.; MacPherson, J. V.; Unwin, P. R.; Pollard, A. J.; Roy, D.; Clifford, C. A.; Shiku, H.; Matsue, T.; Klenerman, D.; Korchev, Y. E. *Angew. Chem., Int. Ed.* **2011**, *50*, 9638–9642.

(18) Nijhuis, C. A.; Sinha, J. K.; Wittstock, G.; Huskens, J.n; Ravoo, B. J.; Reinhoudt, D. N. *Langmuir* **2006**, *22*, 9770–9775.

(19) Wang, Y.; Cai, H.; Mirkin, M. V. *ChemElectroChem* **2015**, *2*, 343–347.

(20) Shan, X.; Patel, U.; Wang, S.; Iglesias, R.; Tao, N. J. *Science* **2010**, *327*, 1363–1366.

(21) Lu, J.; Wang, W.; Wang, S.; Shan, X.; Li, J.; Tao, N. J. *Anal. Chem.* **2012**, *84*, 327–333.

(22) Wang, S.; Huang, X.; Shan, X.; Foley, K. J.; Tao, N. J. *Anal. Chem.* **2010**, *82*, 935–941.

(23) Shan, X.; Díez-Pérez, I.; Wang, L.; Wiktor, P.; Gu, Y.; Zhang, L.; Wang, W.; Lu, J.; Wang, S.; Gong, Q.; Li, J.; Tao, N. J. *Nat. Nanotechnol.* **2012**, *7*, 668–672.

(24) Shan, X.; Wang, S.; Wang, W.; Tao, N. J. *Anal. Chem.* **2011**, *83*, 7394–7399.

(25) Huang, X.; Wang, S.; Shan, X.; Chang, X.; Tao, N. J. *J. Electroanal. Chem.* **2010**, *649*, 37–41.

(26) Wang, Y.; Shan, X.; Cui, F.; Li, J.; Wang, S.; Tao, N. J. *Anal. Chem.* **2015**, *87*, 494–498.

(27) Wang, W.; Foley, K.; Shan, X.; Wang, S.; Eaton, S.; Nagaraj, V. J.; Wiktor, P.; Patel, U.; Tao, N. J. *Nat. Chem.* **2011**, *3*, 249–255.

(28) Foley, K. J.; Shan, X.; Tao, N. J. *Anal. Chem.* **2008**, *80*, 5146–5151.

(29) Lu, J.; Wang, W.; Wang, S.; Shan, X.; Li, J.; Tao, N. J. *Anal. Chem.* **2012**, *84*, 327–333.

(30) MacGriff, C.; Wang, S.; Wiktor, P.; Wang, W.; Shan, X.; Tao, N. J. *Anal. Chem.* **2013**, *85*, 6682–6687.

(31) Meixner, A. J.; Bopp, M. A.; Tarrach, G. *Appl. Opt.* **1994**, *33*, 7995–8000.

(32) Zayats, A. V.; Smolyaninov, I. I.; Maradudin, A. A. *Phys. Rep.* **2005**, *408*, 131–314.

(33) Chen, Z.; Shan, X.; Guan, Y.; Wang, S.; Zhu, J.-J.; Tao, N. J. *ACS Nano* **2015**, *9*, 11574–11581.

(34) Wang, Y.; Kececi, K.; Mirkin, M. V.; Mani, V.; Sardesai, N.; Rusling, J. F. *Chem. Sci.* **2013**, *4*, 655–663.